ARMY RESEARCH LABORATORY

Wind Noise Suppression for Infrasound Sensors

by John M. Noble, W.C. Kirkpatrick Alberts, II, Sandra L. Collier, Richard Raspet, and Mark A. Coleman

ARL-TR-6873 **March 2014**

NOTICES

Disclaimers

The findings in this report are not to be construed as an official Department of the Army position unless so designated by other authorized documents.

Citation of manufacturer's or trade names does not constitute an official endorsement or approval of the use thereof.

Destroy this report when it is no longer needed. Do not return it to the originator.

Army Research Laboratory
Adelphi, MD 20783-1197

ARL-TR-6873 **March 2014**

Wind Noise Suppression for Infrasound Sensors

John M. Noble, Sandra L. Collier, and Mark A. Coleman
Computational and Information Sciences Directorate, ARL

W.C. Kirkpatrick Alberts, II
Sensors and Electron Devices Directorate, ARL

Richard Raspet
University of Mississippi

REPORT DOCUMENTATION PAGE

Form Approved
OMB No. 0704-0188

1. REPORT DATE *(DD-MM-YYYY)*	2. REPORT TYPE	3. DATES COVERED (From - To)
March 2014	DRI	October 2012 to September 2013

4. TITLE AND SUBTITLE
Wind Noise Suppression for Infrasound Sensors

5a. CONTRACT NUMBER

5b. GRANT NUMBER

5c. PROGRAM ELEMENT NUMBER

6. AUTHOR(S)
John M. Noble, W.C. Kirkpatrick Alberts, II, Sandra L. Collier, Richard Raspet, and Mark A. Coleman

5d. PROJECT NUMBER

5e. TASK NUMBER

5f. WORK UNIT NUMBER

7. PERFORMING ORGANIZATION NAME(S) AND ADDRESS(ES)
U.S. Army Research Laboratory
ATTN: RDRL-CIE-S
2800 Powder Mill Road
Adelphi, MD 20783-1197

8. PERFORMING ORGANIZATION REPORT NUMBER
ARL-TR-6873

9. SPONSORING/MONITORING AGENCY NAME(S) AND ADDRESS(ES)

10. SPONSOR/MONITOR'S ACRONYM(S)

11. SPONSOR/MONITOR'S REPORT NUMBER(S)

12. DISTRIBUTION/AVAILABILITY STATEMENT
Approved for public release; distribution unlimited.

13. SUPPLEMENTARY NOTES

14. ABSTRACT
The porous hose and pipe arrays often used for wind noise suppression in long-term infrasound monitoring arrays can be tedious to install and can significantly alter the signals reaching the infrasound sensors. An ideal windscreen, over the frequency band of interest, should preserve all of the characteristics of desired signals that reach the sensor, while removing all of the wind-generated noise. In order to improve upon current state-of-the-art infrasound windscreens, two porous and one non-porous fabric domes were investigated for use as infrasound wind screens. Both of the porous domes perform well in preserving signal information and in consistently reducing wind-generated noise reaching the sensor.

15. SUBJECT TERMS
Acoustics, Infrasound, Wind Noise, Windscreen

16. SECURITY CLASSIFICATION OF:			17. LIMITATION OF ABSTRACT	18. NUMBER OF PAGES	19a. NAME OF RESPONSIBLE PERSON
a. REPORT	b. ABSTRACT	c. THIS PAGE			John M. Noble
Unclassified	Unclassified	Unclassified	UU	32	19b. TELEPHONE NUMBER (*Include area code*) (301) 394-5663

Contents

List of Figures

List of Tables

Acknowledgment

The authors would like to thank Mr. Jeremy Webster for sharing his experience in porous fabric and porous concrete for use in infrasound windscreens.

INTENTIONALLY LEFT BLANK.

1. Introduction

Infrasound is the area of acoustics that is below the audible region of human hearing, starting at 15–20 Hz. For Army infrasound applications, the frequency range of interest is in the 1–20 Hz band. Unlike audible acoustic detection ranges typical of 5–20 km for most sources, infrasound has the ability to propagate extremely long ranges of 100–500 km and, in some cases, much further. For infrasound, one of the primary sources of noise is wind noise. Wind noise, generated by the passage of turbulent air over the microphone, is often suppressed by a windscreen comprised of four to six nominally 20-ft lengths of porous hose radiating out from the microphone. This windscreen has limited the ability to collect infrasonic signatures in covert areas and to deploy arrays in areas where there is limited available space. For both military applications and environmental remote sensing studies, it lacks portability. Physically, the porous hoses are acting as integrated spatial filter. While there are other developmental windscreens, none have been fully demonstrated and documented. This report presents the results of a theoretical and experimental examination of alternative windscreens, specifically porous and non-porous polymer fabrics stretched in dome configurations.

For audible frequency acoustics, the typical windscreen is a sphere made of a porous material that integrates the small-scale turbulent fluctuations, leaving a near laminar flow at the center of the windscreen. From Kolmogorov (*1*), the turbulence velocity spectra (figure 1) are separated into frequency ranges. These ranges are typically expressed as three spatial scales of turbulence source region (large scale), inertial subrange (intermediate scale), and dissipation region (small scale). For infrasound, the region of interest for wind noise generation is the source region, and the low frequency part of the inertial sub-range, which is comprised of large eddies with length scales of tens of meters to kilometers. Unlike higher frequency turbulence, the infrasound region is not isotropic and not homogeneous.

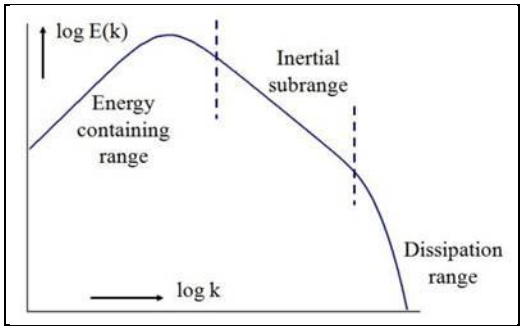

Figure 1. The Kolmogorov turbulence spectrum.

In the early 2000s, Liszka (*2*), Hedlin and Raspet (*3*), and Bedard et al. (*4*) separately showed that wind barriers could be used for infrasonic wind noise reduction. Wind barriers break up

turbulence and effectively perform a spatial average on turbulence scales smaller than the size of the barrier. In these studies, a large wooden structure, such as in figure 2a, was constructed around the infrasound sensor or, in Bedard's case, a porous screen fence was used (figure 2b). The results of these studies showed equivalent wind noise reduction levels as the ported pipes being used at the time for Infrasound Monitoring Stations (IMS). The research has continued to study different designs to include size, materials, and extensions, such as the serrated edges first used by Bedard to break up the turbulent flow coming over the top of the wind barrier. These ideas and designs were some of the inspirations behind the design of the fabric dome used in this research project.

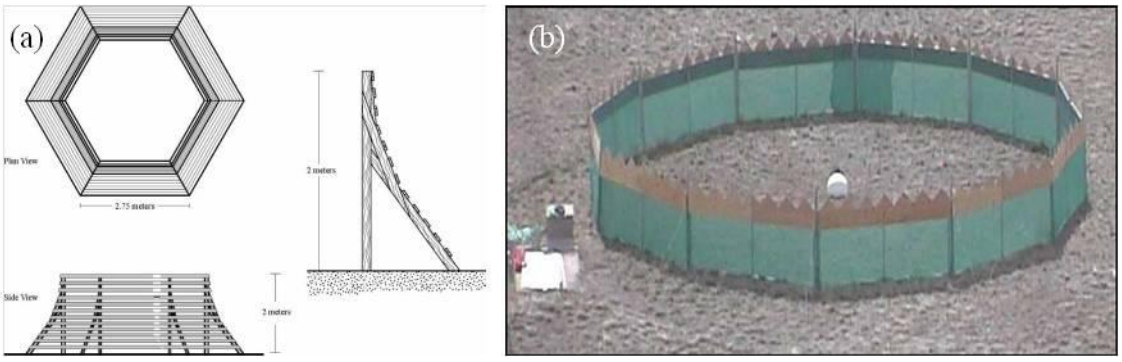

Figure 2. Wind barrier designs used by Liszka, Hedlin, and Raspet (a) and Bedard (b).

The following section presents a theoretical development of the wind noise production in three regions inside and outside an infrasound windscreen. Experimental procedures are given in section 3. An analysis of experimental and theoretical results is given in section 4. Section 5 offers some concluding remarks.

2. Theory

The one-dimensional turbulent kinetic energy spectrum is given by (5)

$$E(k) = C\varepsilon^{2/3}k^{-5/3} \ , \tag{1}$$

where ε is the energy dissipation rate of turbulent energy per unit mass, C is the Kolmogorov constant for a one-dimensional spectrum, which typically ranges from 1.4 to 1.8, and k is the wavenumber. The energy dissipation rate is calculated using

$$\varepsilon = \sqrt{\frac{1}{2}(\sigma_u^2 + \sigma_v^2 + \sigma_w^2)} \ , \tag{2}$$

where σ_u^2, σ_v^2, and σ_w^2 are the standard deviations of the $u, v,$ and w components of the wind field, respectively. Figure 3 shows the turbulent kinetic energy spectrum for the three wind

conditions used in the present analysis of the wind noise measurements. It shows that as the wind speed increases, the variance in the wind field generally increases, providing more turbulent energy. This results in an increase in the wind noise detected by the infrasound microphone.

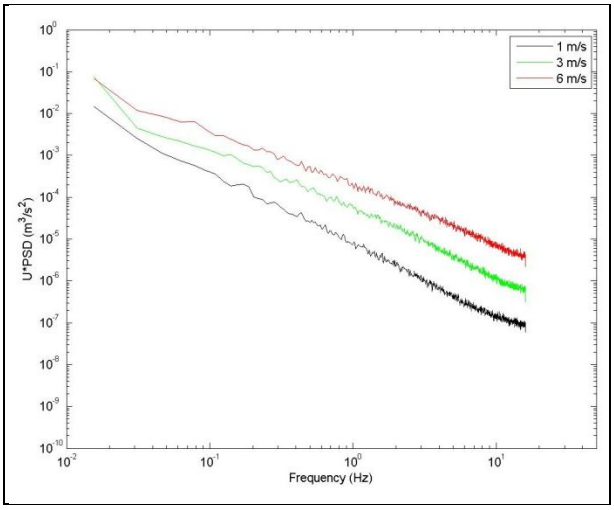

Figure 3. The turbulent kinetic energy spectrum for low, medium, and high wind conditions.

For low frequency acoustics, the wind noise contributions due to turbulence have been shown to be divided into turbulence-sensor, turbulence-turbulence, and turbulence-mean shear interactions (*6*). Recently, these models have been extended to include contributions in the source region of the turbulence spectrum (*7*–*9*). The stagnation pressure is a result of the pressure imparted on an object due to the deflection of the wind around the object. The fluctuations within the wind field will result in a fluctuating stagnation pressure on the sensor. The stagnation pressure power density (P_s) due to the turbulence-sensor interaction is

$$P_s(k_1) = \frac{1.44\bar{u}^2 C}{[1+(k_1\lambda)^2]^{5/6}} + \frac{1.451C^2}{\lambda\,[1+0.1129(k_1\lambda)^2]^{5/6}}\,, \tag{3}$$

where k_1 is the wavenumber in the wind direction ($k_1 = 2\pi f/\bar{u}$) and $\overline{u}$ is the average wind speed. The fitting parameters C and λ are derived from the one-dimensional downwind velocity spectrum in a free jet

$$V_{11}(k_1) = \frac{C}{[1+(k_1\lambda)^2]^{5/6}} \tag{4}$$

using k_1 calculated from the above and fitting to the measured velocity spectrum. This can be used based on Taylor's frozen turbulence hypothesis, which states the turbulent wind field is frozen in time and is transported past the sensor at the mean wind speed, $\overline{u}$. This is considered valid since the lifetime of a turbulent eddy is long compared to the time of passage by the sensor. Stagnation pressure is the pressure measured at the zero velocity position on a rigid sphere and is independent of the radius. This formulation developed by Raspet et al. (*8*) extends the previous

formulation for the stagnation pressure, which was only valid in the inertial sub-range, down into the source region of the turbulence spectrum.

The next source of noise is a result of pressure anomalies generated due to the interaction between turbulent eddies. This effect is referred to as the turbulence-turbulence interaction and is independent of the presence of an object. For the inertial sub-range, this noise is the dominant source. The pressure power spectral density for the turbulence-turbulence interaction (P_t) is

$$P_t(k_1) = 0.811 \frac{C^2}{\lambda} \frac{1}{[1 + 0.1792(k_1\lambda)^2]^{7/6}} . \quad (5)$$

This form of the equation has the modifications made by Raspet et al. (*8*) to extend it into the source region, which is the dominant source of turbulence for infrasound. For low wavenumbers (large scale turbulence), the turbulence-turbulence interaction is a constant.

Finally, the vertical gradient of the wind field near the surface of the earth dampens turbulent eddies being generated in this region and results in a noise known as the turbulence-mean shear interaction. The pressure power spectral density for the turbulence-mean shear interaction (P_m) is

$$P_m(k_1) = 7.38\, CK^2 \frac{\lambda^2 (k_1\lambda)^{5/3}}{[1 + 1.622(k_1\lambda)^2]^{8/3}} , \quad (6)$$

where *K* is the gradient of the average wind speed at the observation height. Unlike for the first two interactions, the spectrum at low wavenumbers is not constant. Instead, the spectrum increases as ${k_1}^{5/3}$, peaks just before the transition to the inertial sub-range, and then decays as ${k_1}^{-11/3}$.

Based on work by Raspet et al. (*8*), Yu et al. (*7*, *9*, *10*), and Abbott et al. (*11–13*), a model was developed to determine the pressure at the center of a wind barrier or wind screen. The pressure (P_c) can be calculated by summing the pressure contributions due to atmospheric turbulence from each of the three regions of the wind screen: inside (P_1), boundary (P_2), and outside (P_3). These regions are shown in the sketch in figure 4, which depicts wind flow around a hemisphere placed on the ground. The summed pressure, P_c, is expressed as

$$P_c^2 = P_1^2 + P_2^2 + P_3^2 . \quad (7)$$

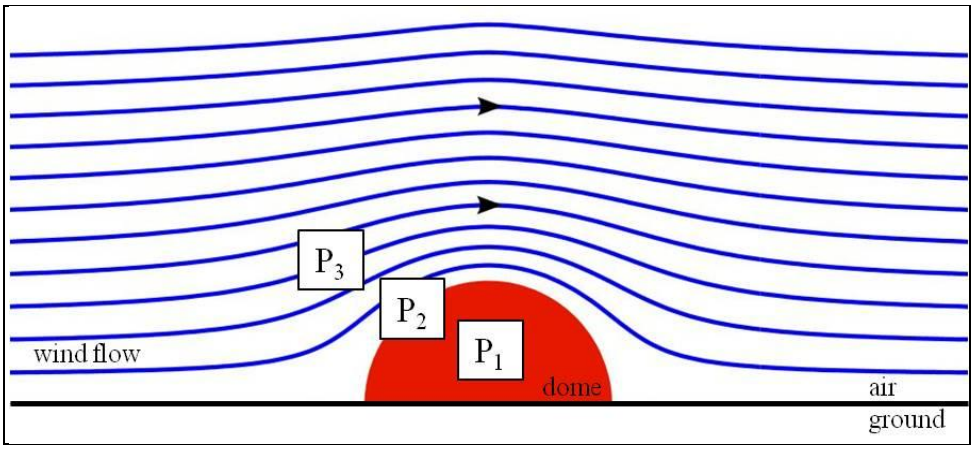

Figure 4. Sketch of the wind flow around a hemisphere placed on the ground.

Starting at Region 1, which is the interior of the porous fabric dome, the wind field will be greatly reduced due to passage through the porous wind barrier. Abbott (*12*) suggests modeling the interior wind field gradient by a summation of exponentials

$$u = u_0 \left(1 - \sum_{i=0}^{n} A_i e^{-\beta_i z}\right), \tag{8}$$

where A_i and β_i are fitting parameters, and z is the height above the surface. It is assumed the dome will eliminate the stagnation pressure, thus leaving the residual wind noise contributions to be the turbulence-turbulence and turbulence-mean shear interactions.

Yu (*10*) derives the pressure (p) due to wind noise at the center of the wind barrier by starting with the source equation for the pressure fluctuations due to the turbulence-mean shear interaction

$$\nabla^2 p(\vec{r}, t) = -2\,\rho_0 \frac{s(z)\partial \tilde{V}_z}{\partial x}. \tag{9}$$

Here $\vec{r} = (x, y, z)$ is the coordinate vector where x corresponds to the flow direction, y is transverse to the flow (x, y are in the horizontal plane), and z is vertical. Additionally, ρ_0 is the density of air, $s(z) = dU_x/dz$ is the vertical gradient of the mean wind velocity along the direction of flow, and $\tilde{V}_z$ is the vertical turbulent velocity component. Applying the boundary condition that the pressure is zero at the surface and at infinity gives

$$p(z, \vec{\kappa}, \omega) = \frac{1}{2\kappa} \int_0^{\infty} e^{-\kappa|z'-z|} T(z', \vec{\kappa}, \omega) dz' + \frac{1}{2\kappa} e^{-\kappa z} \int_0^{\infty} e^{-\kappa z'} T(z', \vec{\kappa}, \omega) dz', \tag{10}$$

where $T(z', \vec{\kappa}, \omega)$ is the Fourier transform of the source function $T(\vec{x}, t) = -\frac{2\rho_0 s(z)\partial \tilde{V}_z}{\partial x}$, and $\vec{\kappa} = k_x \hat{e}_x + k_y \hat{e}_y$ is the wave vector in the plane parallel to the bounding surface (horizontal

plane). Using the exponential form for the wind velocity profile shown in equation 8 and the Fourier transform of the velocity correlation tensor applied for $z = 0$ yields

$$|p(0,\vec{\kappa}\,)|^2 = \frac{2\rho_0^2 k_x^2}{\pi} \times \sum_{i=0,j=0}^{i=n,j=n} s_i s_j \int_{-\infty}^{\infty} \frac{E(k)}{k^4} dk_z \int_0^{\infty} e^{-(\kappa+\beta_i)z'} \sin(k_z z')\, dz' \int_0^{\infty} e^{-(\kappa+\beta_j)z} \sin(k_z z)\, dz\,, \tag{11}$$

where $E(k)$ is the velocity spectrum function given by

$$E(k) = \frac{55C}{18} \frac{(k\lambda)^4}{[1 + (k\lambda)^2]^{17/6}}. \tag{12}$$

Substituting this into equation 11 results in

$$|p_1(0,k_x)|^2 = \frac{440C\lambda^4\rho_0^2 k_x^2}{9\pi} \times \sum_{i=0,j=0}^{i=n,j=m} s_i s_j \iint_0^{\infty} \frac{dk_z dk_y}{[1 + (k\lambda)^2]^{17/6}} \int_0^{h} e^{-(\kappa+\beta_i)z} \sin(k_z z)\, dz \int_0^{h} e^{-(\kappa+\beta_j)z'} \sin(k_z z')\, dz' \tag{13}$$

for the interior of the fabric dome, where h is the height of the wind barrier, ρ_0 is the air density, and β_i and β_j are fitting parameters. The wavenumber is $k = \sqrt{k_x^2 + k_z^2 + k_y^2}$, and the wavenumber for the horizontal-plane projection is $\kappa = \sqrt{k_x^2 + k_y^2}$.

The next region is the undisturbed flow impinging on the fabric dome. In this region, the wind velocity profile is assumed to be a typical logarithmic profile, $u = \frac{u_*}{k_v} \ln\left(\frac{z}{z_0}\right)$ where u_* is the friction velocity, k_v is the Von Karman constant (0.41), and z_0 is the surface roughness. The friction velocity can be calculated using

$$u_*^4 = \langle uw\rangle^2 + \langle vw\rangle^2, \tag{14}$$

where $\langle uw\rangle$ and $\langle vw\rangle$ are shearing stresses at the surface for the momentum fluxes of the wind field. Like in Region 1, the wind noise contribution in Region 3 can be calculated from the measured turbulence and velocity profile. Going through the same process as before except using a logarithmic profile,

$$u(z) = a\, ln\left(\frac{z}{z_0}\right), \tag{15}$$

instead of an exponential profile and using the trigonometric function difference relations results in

$$|p(0,\vec{\kappa},\omega)|^2 = \frac{2\,a^2\,\rho_0^2 k_x^2}{\pi^2}\int_{-\infty}^{\infty}\frac{E(k)}{k^4}dk_z\int_0^{\infty}\frac{e^{-\kappa z}\sin(k_z z)}{z}dz\int_0^{\infty}\frac{e^{-\kappa z'}\sin(k_z z')}{z'}dz'\,, \tag{16}$$

where a is a scaling parameter determined by the wind profile. Substituting equation 12 gives

$$|p_3(0,k_x)|^2 = \frac{440a^2C\lambda^4\rho_0^2k_x^2}{9\pi}\times \iint_0^{\infty}\frac{dk_z dk_y}{[1\ +\ (k\lambda)^2]^{17/6}}\int_0^{\infty}\frac{e^{-\kappa z}\sin(k_z z)}{z}dz\int_0^{\infty}\frac{e^{-\kappa z'}\sin(k_z z')}{z'}dz'. \tag{17}$$

The final region is Region 2, which contains the surface of the porous fabric dome. Here the stagnation pressure and the turbulence-mean shear interactions are the dominant sources to the wind noise. Currently, there is only an empirical model to estimate the contribution to the wind noise for this region (*12*). The model will estimate the wind noise based on the mean wind velocity, wind gradient, and correlation length inside/outside the dome, and on the measured incident turbulent field. Starting with the Green's function solution to the Poisson equation for an incompressible fluid, the pressure fluctuation at the surface of the dome can be calculated (*14*). The solution for the instantaneous static pressure is

$$p(\vec{r},t) = -\frac{\rho_0}{4\pi}\int\frac{q(\vec{r}',t)}{|\vec{r}'-\vec{r}|}\,d^3\vec{r}'\,, \tag{18}$$

where $q(\vec{r}',t)$ is the source term in a free shear flow. Applying the Fourier transform to the Green's function and converting to spherical coordinates yields

$$p_2(0,k) = -\frac{\rho_0}{4\pi}\int\frac{Q(r,\theta,\phi,k)}{r}r^2\sin\theta dr d\theta d\phi\,, \tag{19}$$

where $Q(r,\theta,\phi,k)$ is the Fourier transform of the source term, which can be written as

$$Q(r,\theta,\phi,k) = iku(r,\theta,\phi,k)S(\theta,\phi)\,. \tag{20}$$

The term $S(\theta,\phi)$ represents the wind velocity gradient across the dome's surface and can be written as

$$S(\theta,\phi) = \frac{\Delta u}{\delta}\,, \tag{21}$$

where Δu is the measured difference in the wind velocity on each side of the dome surface, and δ is the boundary layer thickness shown in figure 5. The term $iku(r,\theta,\phi,k)$ is a product of the wavenumber, with the wind velocity turbulence spectrum impinging on the surface of the dome.

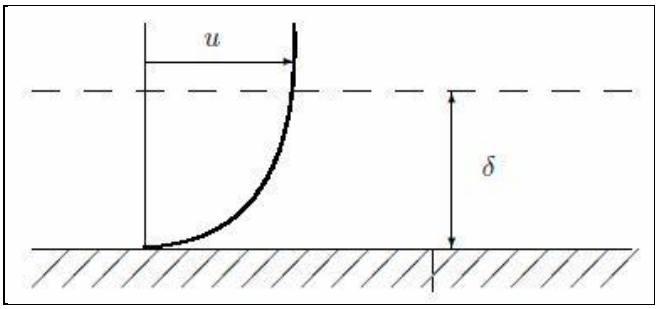

Figure 5. The boundary layer developed by the wind flow over the dome.

The wind velocity spectrum $F(k)$ is determined by performing a curve fit of the measured spectrum to the von Karman spectrum for a free jet

$$F(k) = \frac{C}{[1 + (k\lambda)^2]^{5/6}} \ . \tag{22}$$

Substituting equation 20 into equation 19 yields

$$p_2(0,k) = -\frac{ik\rho_0}{4\pi}\int u(r,\theta,\phi,k)S(\theta,\phi)\, r\, \sin\theta dr d\theta d\phi \ . \tag{23}$$

Assuming that the pressure at the center of the dome is dominated by the thin surface layer ($dr \to \delta$), equation 23 may be reduced to the surface integral

$$p_2(0,k) = -\frac{ik\rho_0 r_0 \delta}{4\pi}\int_0^{2\pi}\int_0^{\frac{\pi}{2}} u(r_0,\theta,\phi,k)S(\theta,\phi)\sin\theta d\theta d\phi \ , \tag{24}$$

where r_0 is the radius of the dome.

Finally, the power spectrum for the pressure is calculated by taking the product of p_2 with its complex conjugate giving

$$|p_2(0,k)|^2 = \frac{k^2\rho_0^2 r_0^2 \delta^2}{16\pi^2} \times \int_0^{2\pi}\int_0^{\frac{\pi}{2}}\int_0^{2\pi}\int_0^{\frac{\pi}{2}} S^*(\theta',\phi')S(\theta,\phi)\langle u^*(r_0',\theta',\phi',k)u(r_0,\theta,\phi,k)\rangle \sin\theta' \sin\theta d\theta' d\phi' d\theta d\phi \ , \tag{25}$$

where $\langle u^*(r_0',\theta',\phi',k)u(r_0,\theta,\phi,k)\rangle$ is defined as the cross-correlation of the wind fluctuations. Studies conducted by Priestley (*15*) shows that the cross-correlation can be rewritten as the velocity power spectrum times an exponential decay or

$$\langle u^*(r_0', \theta', \phi', k) u(r_0, \theta, \phi, k) \rangle = u^*(k) u(k) e^{-\alpha(k) r_0 \sqrt{(\theta' - \theta)^2 + \sin^2 \theta \, (\phi' - \phi)^2}} , \tag{26}$$

where the attenuation coefficient, $\alpha(k)$, is related to the inverse of the correlation length. Priestley (*15*) and Shields (*16*) showed that the attenuation coefficient could be expressed in the form $\alpha(k) = \mu k^q$, where μ and q are fitting parameters dependent on the porosity of the material. Table 1 shows the values for μ and q determined by Abbott (*12*) for a number of wall porosities.

Table 1. The values for the fitting parameters $\boldsymbol{\mu}$ and $\boldsymbol{q}$ for different fabric porosities.

Porosity	μ	q
30%	1.0304	0.7674
40%	1.4142	0.6545
55%	1.6976	0.6076
65%	1.2786	0.7601
80%	1.5166	0.6681

Substituting equation 26 into equation 25 results in

$$|p_2(0,k)|^2 = \frac{k^2 \rho_0^2 r_0^2 \delta^2}{16\pi^2} \int_0^{2\pi} \int_0^{\frac{\pi}{2}} \int_0^{2\pi} \int_0^{\frac{\pi}{2}} S^*(\theta', \phi') S(\theta, \phi) \, u^*(k) u(k) \times e^{-\alpha(k) r_0 \sqrt{(\theta' - \theta)^2 + \sin^2 \theta \, (\phi' - \phi)^2}} \sin\theta' \sin\theta \, d\theta' \, d\phi' , \tag{27}$$

where $u(k)$ can be expressed by fitting the wind velocity spectrum to the von Karman spectrum for a free jet (equation 22) which yields

$$|p_2(0,k)|^2 = \frac{k^2 \rho_0^2 r_0^2 \delta^2}{16\pi^2} \int_0^{2\pi} \int_0^{\frac{\pi}{2}} \int_0^{2\pi} \int_0^{\frac{\pi}{2}} S^*(\theta', \phi') S(\theta, \phi) \, \frac{C}{[1 + (k\lambda)^2]^{5/6}} \, \frac{C}{[1 + (k\lambda)^2]^{5/6}} \times e^{-\alpha(k) r_0 \sqrt{(\theta' - \theta)^2 + \sin^2 \theta \, (\phi' - \phi)^2}} \sin\theta' \sin\theta \, d\theta' \, d\phi' \, d\theta \, d\phi. \tag{28}$$

The final term to expand is the product of the velocity gradients at the surface of the dome, $S^*(\theta', \phi') S(\theta, \phi)$. The estimate of the velocity gradient is given in equation 21. As mentioned previously, Δu represent the difference in wind velocity between outside and inside of the dome or $\Delta u = u_{\text{out}} - u_{\text{in}}$. The terms u_{out} and u_{in} are considered to be uniform and unidirectional. As a result, Δu is uniform around the dome for a turbulent boundary layer thickness δ defined by $u = 0.99 u_{\text{out}}$. To model the turbulent boundary layer profile, the one-seventh power-law velocity profile will be used giving

$$\frac{u}{u_{\text{out}}} = \left(\frac{r}{\delta}\right)^{1/7}. \tag{29}$$

Solving for the boundary layer thickness results in

$$\delta = r\left(\frac{u_{\text{out}}}{u}\right)^{7}. \tag{30}$$

Substituting this into equation 21 gives

$$S(\theta,\phi) = \frac{\Delta u}{r}\left(\frac{u}{u_{\text{out}}}\right)^{7} \tag{31}$$

for the velocity gradient at the surface of the dome where r is the normal distance from the surface, u_{out} is the outside measured upwind of the dome, Δu is the difference in wind velocity between outside and inside of the dome, and u is the wind velocity at distance r from the surface of the dome. To determine the ratio u/u_{out}, Abbott (*12*) used the cosine Fourier series

$$\frac{u}{u_{\text{out}}} = A_0 + \sum_{n=1}^{\infty} A_n \cos(n\theta), \tag{32}$$

where A_0 and A_n are coefficients determined from fitting the equation to measurements. Finally, substituting equation 32 into equation 31 yields

$$S(\theta,\phi) = \frac{\Delta u}{r}\left[A_0 + \sum_{n=1}^{\infty} A_n \cos(n\theta)\right]^{7}. \tag{33}$$

Substituting this result into equation 28 gives the final form for the power spectrum for the pressure contribution to the wind noise in Region 2

$$|p_2(0,k)|^2 = \frac{k^2\rho_0^2 r_0^2 \delta^2 C^2}{16\pi^2} \int_0^{2\pi}\int_0^{\frac{\pi}{2}}\int_0^{2\pi}\int_0^{\frac{\pi}{2}} \left(\frac{\Delta u}{r}\right)^2 \frac{[A_0 + \sum_{n=1}^{\infty} A_n \cos(n\theta')]^7}{[1 + (k\lambda)^2]^{5/6}} \times \frac{[A_0 + \sum_{n=1}^{\infty} A_n \cos(n\theta)]^7}{[1 + (k\lambda)^2]^{5/6}} e^{-\alpha(k) r_0 \sqrt{(\theta'-\theta)^2 + \sin^2\theta\,(\phi'-\phi)^2}} \sin\theta' \sin\theta\, d\theta'\, d\phi'\, d\theta\, d\phi. \tag{34}$$

Finally, to compute the total contributions to the wind noise at the center of the dome, equations 28, 13, and 17 can be substituted into equation 7 and converted from wavenumber space to frequency space by multiplying by $\frac{2\pi}{u_n}$, where u_n is the mean wind velocity in the region. This process leads to the following expressions for the pressures in each region

$$|p_1(0,f)|^2 = \frac{880 C \lambda^4 \rho_0^2 k_x^2}{9u_1} \times \tag{35}$$

$$\sum_{i=0,j=0}^{i=n,j=m} s_i s_j \iint_0^\infty \frac{dk_z dk_y}{[1 + (k\lambda)^2]^{17/6}} \int_0^h e^{-(\kappa+\beta_i)z} \sin(k_z z) dz \int_0^h e^{-(\kappa+\beta_j)z'} \sin(k_z z') dz',$$

$$|p_2(0,f)|^2 = \frac{k^2 \rho_0^2 r_0^2 \delta^2 C^2}{8\pi u_2} \int_0^{2\pi} \int_0^{\frac{\pi}{2}} \int_0^{2\pi} \int_0^{\frac{\pi}{2}} \left(\frac{\Delta u}{r}\right)^2 \frac{[A_0 + \sum_{n=1}^\infty A_n \cos(n\theta')]^7}{[1 + (k\lambda)^2]^{5/6}} \times \tag{36}$$

$$\frac{[A_0 + \sum_{n=1}^\infty A_n \cos(n\theta)]^7}{[1 + (k\lambda)^2]^{5/6}} e^{-\alpha(k) r_0 \sqrt{(\theta'-\theta)^2 + \sin^2\theta\,(\phi'-\phi)^2}} \sin\theta' \sin\theta d\theta' d\phi' d\theta d\phi ,$$

$$|p_3(0,f)|^2 = \frac{880 a^2 C \lambda^4 \rho_0^2 k_x^2}{9 u_3} \times \tag{37}$$

$$\iint_0^\infty \frac{dk_z dk_y}{[1 + (k\lambda)^2]^{17/6}} \int_0^\infty \frac{e^{-\kappa z} \sin(k_z z)}{z} dz \int_0^\infty \frac{e^{-\kappa z'} \sin(k_z z')}{z'} dz' ,$$

and the total at the center of the dome

$$|p_c(0,f)|^2 = |p_1(0,f)|^2 + |p_2(0,f)|^2 + |p_3(0,f)|^2 . \tag{38}$$

According to Abbott (*12*), the comparisons made with a variety of porosities under different wind conditions indicated that for low- to mid-level porosities, the noise contribution due to the wind barrier is the most dominant, while the noise contribution due to the flow inside the fence is negligible. Conversely, for the high porosities, the contributions of the pressure fluctuations on the barrier's exterior are negligible, while the inside and outside contributions are the most dominant. The comparisons also show that the dominant noise sources at the center of the wind fence for low wavenumbers are due to the outside flow and the interactions at the surface of the wind fence, while noise contributions from the flow region inside the fence are negligible. This is consistent for all porosities. The dominant noise sources for high wavenumbers, or wavenumbers where the wavelengths are smaller than the size of the wind fence height, are due principally to the interactions at the surface of the fence for low porosities, while for high porosities the dominant noise source is due to the flow interactions inside the wind fence. Figure 6 shows Abbott's measured pressure spectra inside and outside of his wind fence compared to the theoretical predictions. Figure 6a shows the contributions to the pressure spectra from each of the three regions, and figure 6b shows how the summation of the predicted pressure spectra compared to the measured spectra inside and outside the wind fence. Abbott's model shows very good agreement to the measured spectrum for this case. The largest contribution to the overall wind noise is shown in figure 6a to be from Regions 2 and 3. This case was chosen due to the porosity of the material being close to one of the porosities used in this study.

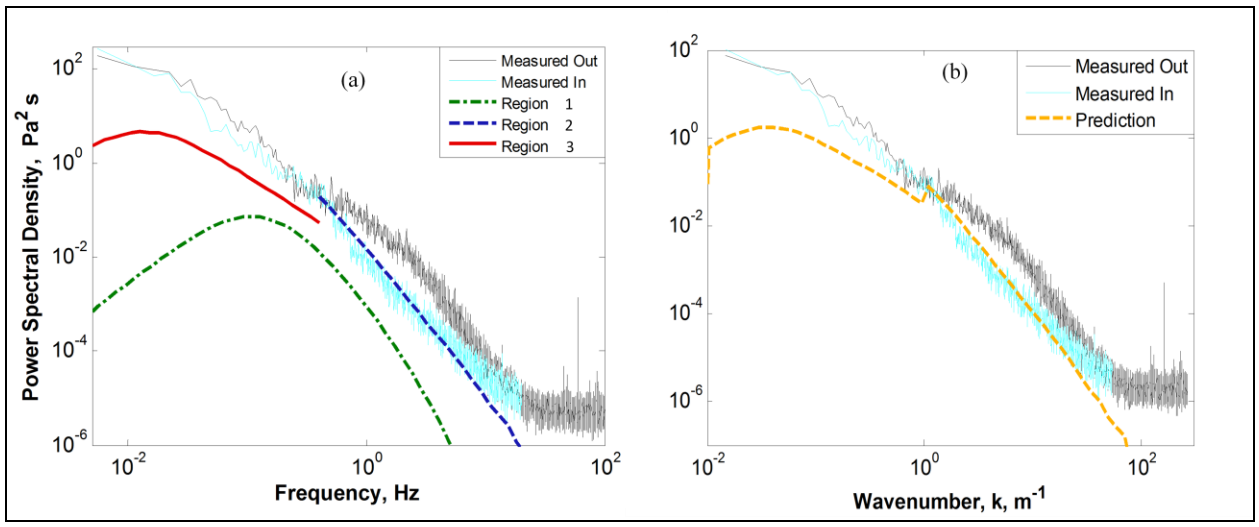

Figure 6. Abbott's measured and predicted pressure spectra for a wind fence with an open top and 30% wall porosity.

3. Experimental Procedures

To investigate the ability of three fabric domes to successfully mitigate wind noise in the infrasonic range, the following procedures were employed. At a U.S. Army test facility, the three domes were placed close to one another and at an angle to the prevailing winds so that turbulent eddies generated by the passage of wind over one of the domes would not artificially increase the wind noise at a downstream dome (figure 7). Hyperion IFS-3000 infrasound sensors (the numbered H's in figure 7b) and Chaparral Model 2 infrasound sensors (the numbered C's in figure 7b) were placed at the center of each dome. Exterior to the domes were two IFS-3000 sensors and one Chaparral Model 2. The Chaparral and one of the IFS-3000 sensors were equipped with a 20-ft radius porous hose rosette. The remaining IFS-3000 was equipped with a high-frequency shroud (HFS) (figure 7c) infrasound windscreen and will be referred to as the HFS-only sensor in subsequent discussions. The three IFS-3000 sensors in the domes were also equipped with HFS windscreens. All signals from the infrasound sensors were recorded using RefTek 130 data recorders sampling at 1 kHz. Only the internal filters in the RefTek analog-to-digital converters were used to low-pass filter the infrasound signals at the Nyquist frequency.

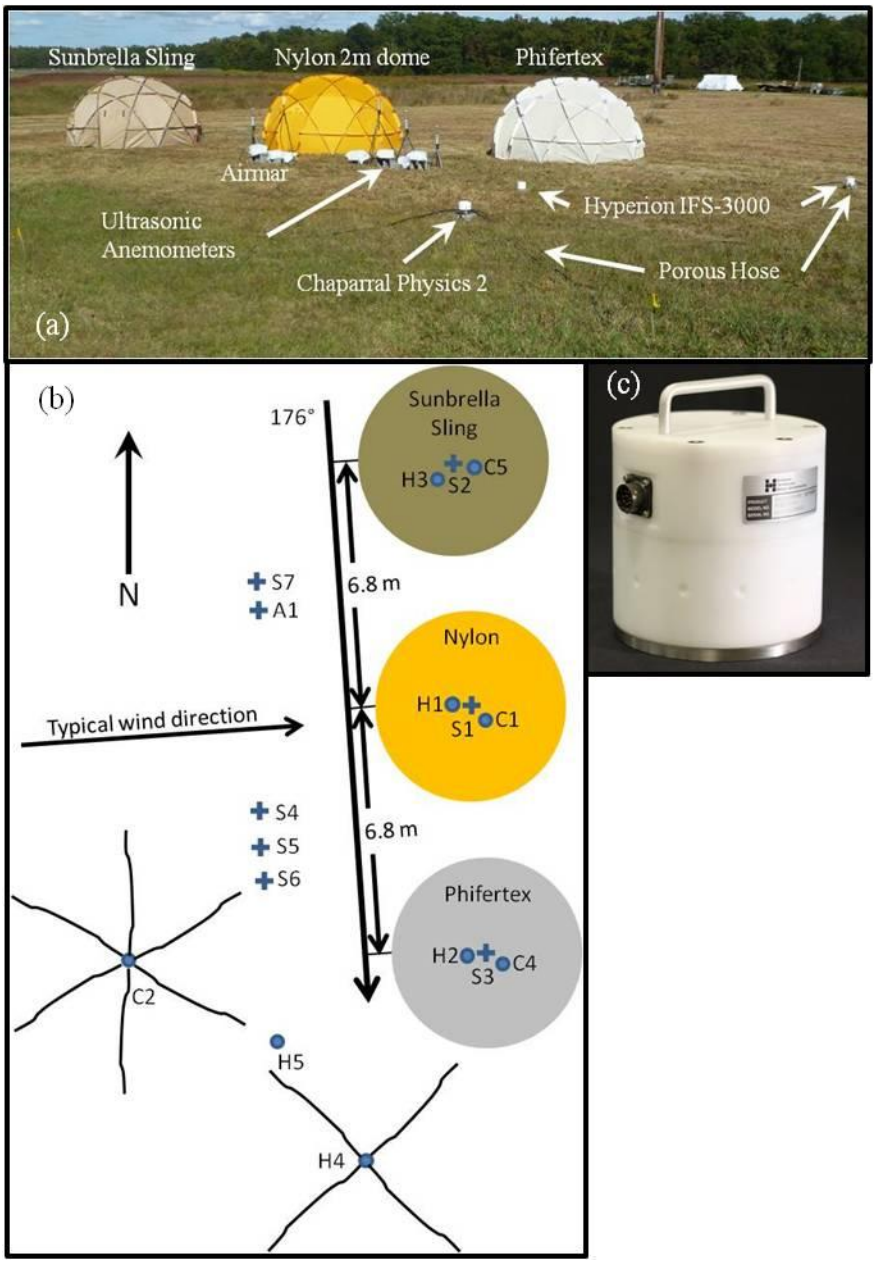

Figure 7. Photograph (a) and overhead sketch (b) of the experimental configuration, and IFS-3000 with high-frequency shroud (HFS) (c).

To monitor the three-dimensional air motion interior and exterior to the domes, R.M. Young model 2000 ultrasonic anemometers (the numbered S's in figure 7b) were used: one in each dome and four outside the domes. The ultrasonic anemometer measures the $u, v,$ and w components of the wind velocity and sonic temperature at a sample rate of 33 Hz. Three of the exterior anemometers were arranged in descending height (166, 123, and 93 cm, labeled by S4 through S6, respectively, in figure 7b) to be able to monitor the vertical distribution of turbulence (*12*) and one, S7, was placed at the same height as S5 to monitor the horizontal variation of the turbulence flow incident on the domes. An Airmar 150WX, A1 in figure 7b, at a height of

159 cm, was used to collect horizontal wind speed, wind direction, temperature, barometric pressure, and relative humidity at a sample rate of 1 Hz. The entire experimental setup collected data for approximately six weeks in order to maximize the chances of wide variations in meteorological conditions and to collect a variety of impulsive signatures.

The dome shape chosen for this investigation is based upon a commercially available 2 m radius tent, which was used as the non-porous dome and is referred to as the Nylon dome. Evidence has been presented (*13*) that a porosity of approximately 40% works well for infrasound windscreen materials. As such, two porous fabrics were chosen to verify the observations made in Abbott et al. (13); one fabric had an approximate porosity of 10% (Sunbrella Sling) and another had an approximate porosity of 35% (Phifertex). Both porous fabrics are vinyl-coated polymer strands, but they have been woven in such a fashion as to be porous. Figures 8a and b show close-up photographs of each fabric. The difference in porosity is clearly visible in the figure. In the following discussion, the domes constructed from each fabric will be referred to by the trade name of the fabric.

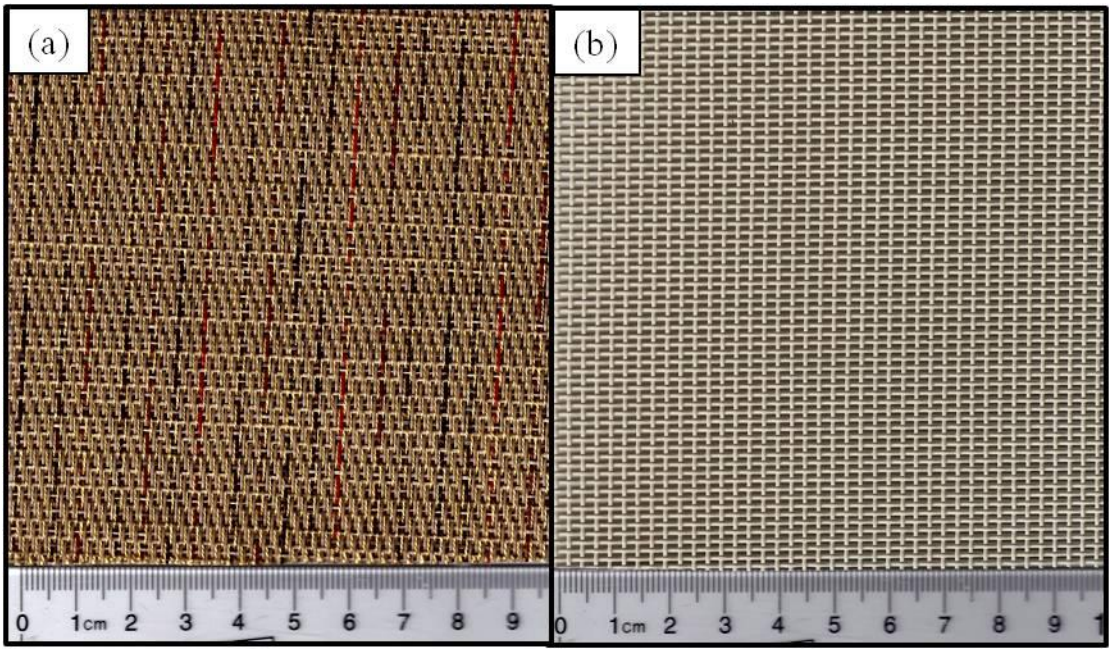

Figure 8. Fabrics used in the construction of the porous domes; Sunbrella Sling (a) and Phifertex (b).

4. Results and Analysis

In order to determine the best data to use in quantifying the wind noise reduction characteristics of each of the domes, the wind speed and direction reported by the Airmar sensor were observed to identify times when the wind direction was ±45° from a line perpendicular to the line joining the three domes, figure 7b. The wind speeds during these times were then used to further

separate the data into time segments, where the wind speed fell into three regions: less than 3 m/s (low), between 3 and 6 m/s (medium), and greater than 6 m/s (high). The power spectral density (PSD) of each infrasound sensor was then computed using Welch's average periodogram method (*17*). Figure 9 (low wind conditions), figure 10 (medium wind conditions), and figure 11 (high wind conditions) depict the PSD of each of the wind noise reduction schemes (a) and the difference between each PSD and the PSD of the HFS-only sensor (b).

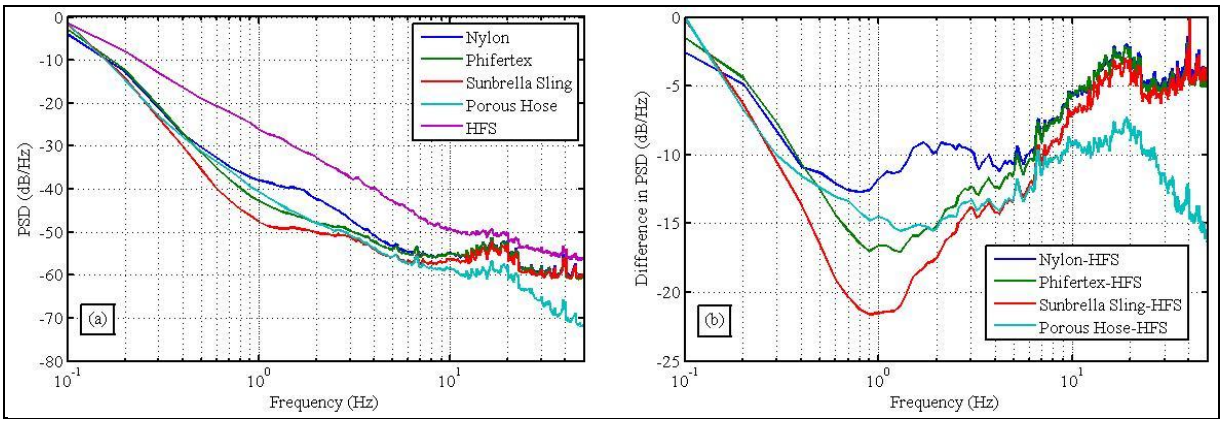

Figure 9. PSDs (a) of the Nylon (blue), Phifertex (green), Sunbrella Sling (red), porous hose (cyan), and HFS (purple) wind noise reduction methods in the low wind condition (speed less than 3 m/s). The difference between the PSDs of the Nylon (blue), Phifertex (green), Sunbrella Sling (red), porous hose (cyan) reduction methods and the HFS are shown in b.

It is readily observed in figure 9a (low wind conditions with wind speeds less than 3 m/s), that below roughly 0.4 Hz, the Nylon (blue), Phifertex (green), and Sunbrella Sling (red) domes tend to reduce the wind noise relative to the HFS-only sensor (purple) by a similar amount to the porous hose (cyan). Between 0.4 and 4 Hz, the Phifertex and porous hose perform roughly the same, while the Sunbrella Sling further reduces the wind noise by 5 dB/Hz. In the same frequency range, the reduction due to the Nylon dome decreases to approximately 1.75 Hz. Between 4 and 10 Hz, the reductions by all of the methods except the HFS are within 5 dB/Hz of each other. Above 10 Hz, the reduction due to the domes remains the same, while the reduction due to the porous hose continues to increase. These differences between the reduction methods are made more apparent when the PSD of the HFS-only sensor is subtracted from the PSDs of the other methods, as shown in figure 9b.

Figure 10a shows PSDs of each of the reduction methods in the medium wind condition, 3–6 m/s. The color designations are the same as in figure 9. As expected, all of the PSDs in figure 10a have increased in magnitude, and some of the features mentioned in the discussion of figure 9a are becoming more apparent. Specifically, the increase in the PSD of the Nylon tent centered at roughly 1.75 Hz, and the similarity between the reduction due to the porous hose and the Sunbrella Sling dome is more apparent. In this medium wind condition, however, the Sunbrella Sling dome maintains its noise reduction capabilities at frequencies above 10 Hz, while the Nylon and Phifertex domes and the porous hose exhibit a decrease in their noise

reduction capabilities. The Phifertex dome begins to significantly deviate from the Sunbrella Sling dome at roughly 6 Hz. This is reinforced by the differences shown in figure 9b, where the Phifertex and Sunbrella Sling domes have PSDs within 5 dB/Hz from 0.1 to 6 Hz, and the Sunbrella Sling dome and the porous hose array remain within 5 dB/Hz of each other from 0.1 Hz and 10 Hz.

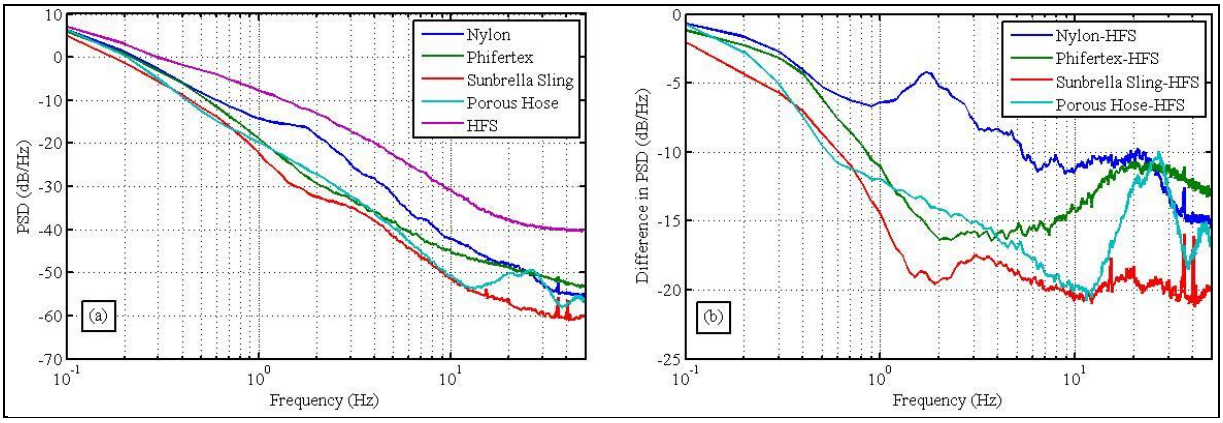

Figure 10. PSDs (a) of the wind noise reduction methods for the medium wind condition (speeds from 3–6 m/s) and differences between the PSD of each method and the PSD of the HFS (b). Color designations are the same as in figure 7.

Figure 11a shows PSDs of each of the wind noise reduction schemes in the high wind condition, speeds greater than 6 m/s. Between 0.1 and 1 Hz, all of the reduction schemes are within 5 dB/Hz (figure 11b). Above 1 Hz, the HFS-only sensor and the Nylon dome significantly deviate from the remaining three reduction schemes. The Phifertex dome, until 8 Hz, stays within 3 dB/Hz of the Sunbrella Sling dome. For the porous hose, this frequency range extends to roughly 10.5 Hz.

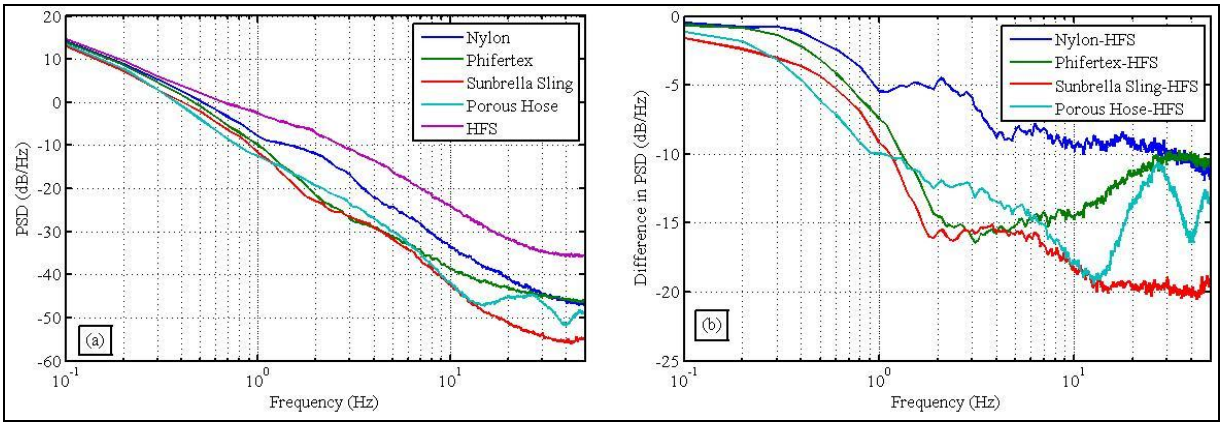

Figure 11. PSDs (a) of the wind noise reduction methods for the high wind condition (speeds greater than 6 m/s) and differences between the PSD of each method and the PSD of the HFS (b). Color designations are the same as in figure 7.

Figure 12 shows the turbulence spectra outside (blue) and inside the Nylon (green), Phifertex (cyan), and Sunbrella Sling (purple) domes for each of the wind conditions: low (a), medium (b), and high (c). The red line in each plot is the theoretical Kolmogorov –5/3 turbulent kinetic energy spectrum for the incident turbulent field. In figure 12, as might be expected, it is observed that the incident turbulence spectrum increases as the wind speed increases. This is also true of the turbulence spectrum inside the Phifertex dome, although the dome maintains an order of magnitude reduction in the turbulence relative to the incident spectrum. The turbulence spectra inside both the Nylon and Sunbrella Sling domes do not behave in as predictable a fashion as the Phifertex dome. If figures 12a through 12c are compared, it is noted that for frequencies above 0.5 Hz the spectrum inside the Sunbrella Sling dome remains relatively constant regardless of exterior wind speed. At lower frequencies, the turbulence spectrum increases with wind speed. Throughout figure 12, the turbulence spectrum inside the Sunbrella Sling dome has a curved shape the cause of which is not known at this time. In figure 11a, the turbulence spectrum of the Nylon dome linearly decreases at a slope slightly less negative than the theoretical –5/3. As the wind speed increases, figure 11b and 11c, the turbulence spectrum inside the Nylon dome assumes a curved shape similar to that inside the Sunbrella Sling dome. At the highest wind speeds, the reason for the odd shape of the lower frequency portion of the spectrum is not known.

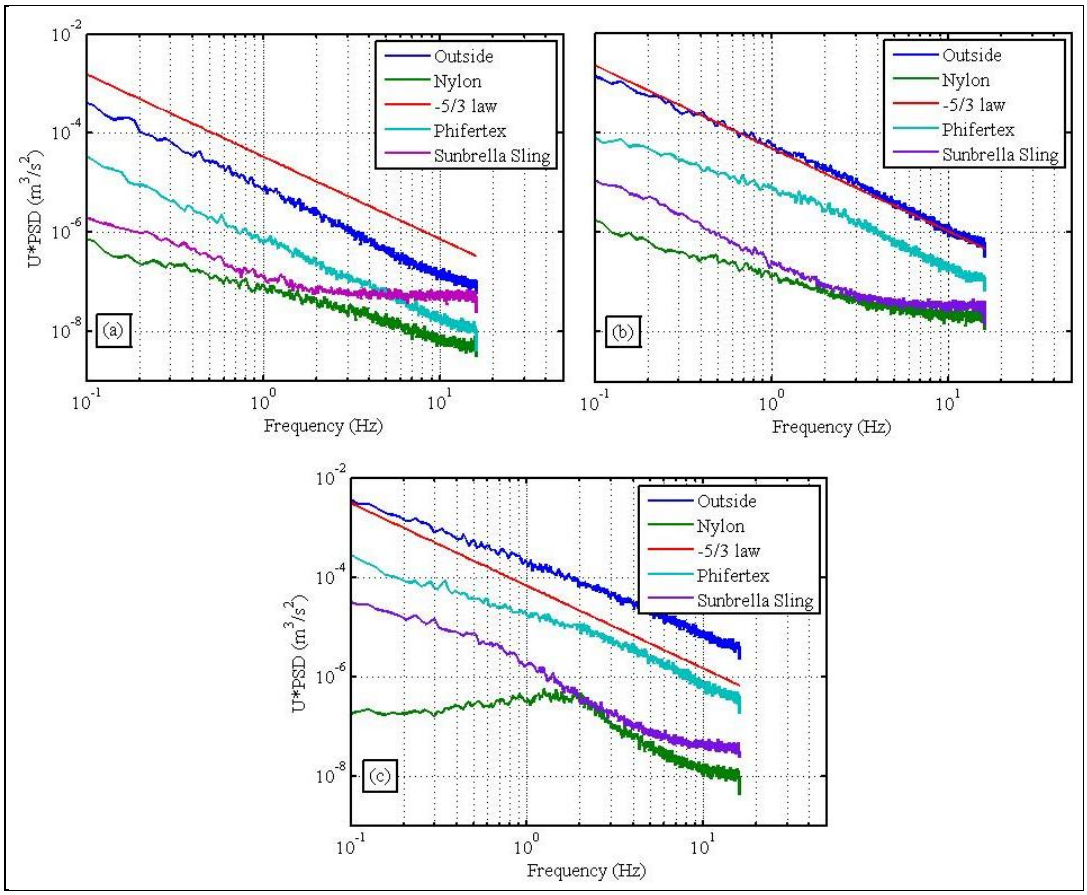

Figure 12. Turbulence spectra outside (blue) and inside the Nylon (green), Phifertex (cyan), and Sunbrella sling (purple) domes for the low- (a), medium- (b), and high-wind (c) conditions. The red line in each plot is the theoretical incident turbulent kinetic energy spectrum.

Figure 13 shows a single explosion event (a) captured by all five infrasound sensors, and the average transfer functions (b) of each wind noise reduction method compared to the infrasound sensor with only the HFS installed. In figure 13a, the waveforms have been time-aligned to better show the differences between the recordings. It is apparent in figure 13a that the waveforms recorded under the HFS (taken to be the reference) and the Phifertex and Nylon domes are all similar although the recording in the Nylon dome has higher peak amplitude than the HFS. Also noted is a small decrease in amplitude of the waveform due to the Sunbrella Sling dome and a large decrease in amplitude due to the porous hose that is accompanied by an apparent low-pass filtering of the waveform. This significant decrease in amplitude due to the porous hose potentially results in a decrease in detection range when using porous hose as a wind noise reduction method. The transfer functions in figure 13b were calculated by taking the transfer functions between each wind noise reduction method and the HFS-only sensor due to four similar waveforms and averaging the results. The error bars in figure 13b are at approximate third-octave center frequencies. From 5 Hz to approximately 75 Hz, the Phifertex dome agrees very well with the HFS-only sensor, while the Sunbrella Sling dome attenuates the signal by

approximately 1 dB. Thus, both porous domes perform exceptionally well at preserving the properties of a signal passing through the dome. The transfer function of the Nylon dome below 20 Hz is flat and agrees well with the HFS-only sensor. However, above 20 Hz, the transfer function of the Nylon dome is greater than one, implying an increase in amplitude of the signal reaching the sensor at the center of the dome. The transfer function of the sensor with the porous hose array is roughly 3 dB below the HFS-only sensor at 5 Hz and steadily decreases to 4 dB below at 20 Hz. Above 20 Hz, the response falls rapidly to approximately 12 dB below the HFS-only sensor at about 60 Hz. This shows the low-pass filter effect of the porous hose alluded to in the discussion of figure 13a.

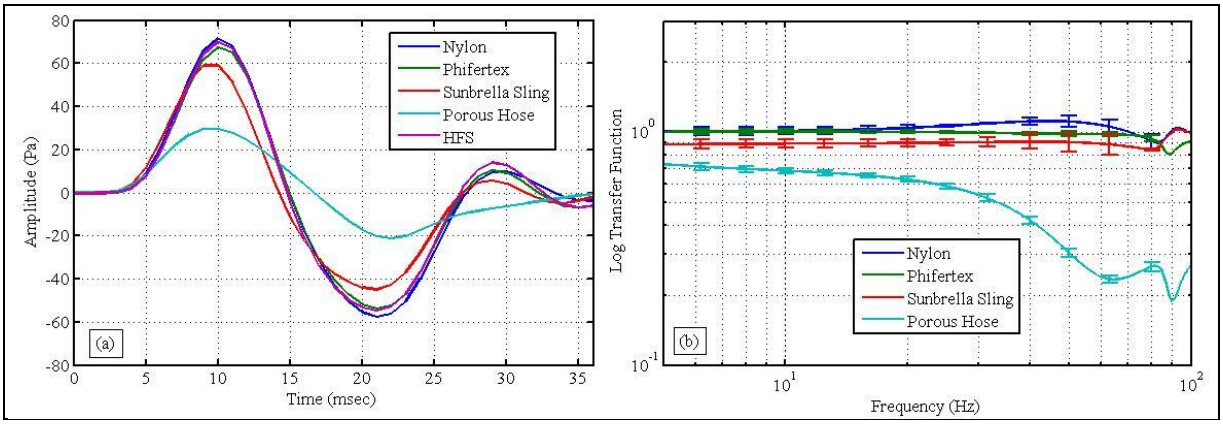

Figure 13. Waveforms of a small explosion (a) and the average transfer functions (b) of each wind noise reduction method relative to the sensor with only the HFS installed.

Based upon the wind noise spectra, the turbulence spectra, and the transfer functions, the porous domes have demonstrated a distinct ability to reduce wind noise at an infrasound sensor and to preserve the characteristics of a signal passing through the wall of the domes. Of the two porous domes, the Sunbrella Sling appears to have the best overall performance: it maximizes the wind noise reduction while losing only a small amount of signal. The Phifertex dome clearly demonstrated the best signal preservation, but its ability to reduce the wind noise reaching the sensor was not sufficiently high at the upper end of the typical frequency range used in Army applications, 1–20 Hz. The non-porous dome introduced too many artifacts, as discussed previously, into the signals to consider it as a viable alternative to porous hose.

5. Concluding Remarks

Two porous fabric and one non-porous fabric domes have been investigated to determine their potential as alternative methods for infrasound wind noise reduction. Transfer functions between a reference sensor and signals measured at the center of the domes or at the center of a porous hose array demonstrated the ability of the porous domes to preserve the information content in a signal. Further, wind noise spectra measured at the center of the domes, when compared to spectra measured by the reference sensor, demonstrated the ability of the domes to reduce the wind noise to a level comparable to that of a porous hose array. Of the two porous domes investigated, the dome constructed from Sunbrella Sling fabric exhibited the best performance and can be considered as a recommended alternative to porous hose rosettes.

6. References

1. Kolmogorov, A. N. Local Structure of Turbulence in an Incompressible Fluid at Very High Reynolds Number. *Dokl Adad Nauk SSSR* **1941**, *30,* 299–303.
2. Liszka, L. *Infrasound: A Summary of 35 Years of Infrasound Research*; Institutet for Rymdfysik, Swedish Institute of Space Physics, IRF Scientific Report 291, Umea, Sweden, 2008.
3. Hedlin, M.A.H.; Raspet, R. Infrasonic Wind-Noise Reduction by Barriers and Spatial Filters. *J. Acoust. Soc. Am.* **2003**, *114* (3), 1379–1386.
4. Bedard, Jr., A. J.; Bartram, B. W.; Keane, A. N.; Welsh, D. C.; Nishiyama, R. T. The Infrasound Network (ISNET): Background, Design Details, and Display Capability as an 88D Adjunct Tornado Detection Tool. *The American Meteorological Society 11th Conference on Aviation, Range, and Aerospace and the 22nd Conference on Severe Local Storms*, October 2004.
5. Stull, R. *An Introduction to Boundary Layer Meteorology*; Kluwer, 1988, 666pp.
6. Walker, K. T.; Hedlin, M.A.H. *A Review of Wind Noise Reduction Methodologies*; in: Infrasound Monitoring for Atmospheric Studies edited by A. Le Pichon, E. Blanc, and A. Hauchecome, Springer, p.141–182.
7. Yu, J.; Raspet, R.; Webster, J.; Abbott, JP. Improved Prediction of the Turbulence-Shear Contribution to Wind Noise Pressure Spectra. J. Acoust. Soc. Am. **2011**, *130* (6), 3590–3594.
8. Raspet, R.; Webster, J.; Dillion, K. Framework for Wind Noise Studies. J. Acoust. Soc. Am. **2006**, *119* (2), 834–843.
9. Yu, J.; Raspet, R.; Webster, J.; Abbott, JP. Wind Noise Measured at the Ground Surface. *J. Acoust. Soc. Am.* **2011**, *129* (2), 622–632.
10. Yu, J. *Calculation of Wind Noise Measured at the Surface under Turbulent Wind Fields*; Ph.D. Thesis, Department of Physics and Astronomy, The University of Mississippi. October 2009.
11. Abbott, JP. R. *The Time Dependent Relationship of Vertical Wind Velocity and Pressure Fluctuations Over Flat Open Ground*; M.S. Thesis, Department of Physics and Astronomy, The University of Mississippi, May 2010.
12. Abbott, JP. R. *Optimization of Wind Fences for Infrasonic Wind Noise Reduction*; Ph.D. Thesis, Department of Physics and Astronomy, The University of Mississippi, May 2014.

13. Abbott, JP. R.; Raspet, R.; Webster, J. Experimental Investigation of Large Porous Wind Fences for Infrasonic Wind Noise Reduction. *J. Acoust. Soc. Am.* **2013**, *134*, 4161.

14. George, W. K.; Beuther, P. D.; Arndt, R.E.A. Pressure Spectra in Turbulent Free Shear Flows. *J. Fluid Mech.* **1984**, *148*, 155–191.

15. Priestley, J. T. *Calculation of the Effectiveness of Infrasound Line Microphones for Reducing Wind Noise*; National Bureau of Standards Report, No. 9380, 1966.

16. Shields, F. D. Low-Frequency Wind Noise Correlation in Microphone Arrays. *J. Acoust. Soc. Am.* **2005**, *117* (6) 3489–3496.

17. Press, W. H.; Flannery, B. P.; Teukolsky, S. A.; Vetterling, W. T. *Numerical Recipes in C: The Art of Scientific Computing*; Cambridge University Press, 1990, p. 401ff.

7. Transitions

Noble, J. M.; Alberts II, W.C.K.; Raspet, R.; Collier, S. L.; Coleman, M. A. Infrasound Wind Noise Reduction Via Porous Fabric Domes. to be presented at the *167th Meeting of the Acoustical Society of America*, Spring 2014.

This DRI research has produced a Cooperative Agreement (W911NF-13-2-0021) with the University of Mississippi through the Army Research Office in May 2013.

1 (PDF)	DEFENSE TECHNICAL INFORMATION CTR DTIC OCA
2 (PDF)	DIRECTOR US ARMY RESEARCH LAB RDRL CIO LL IMAL HRA MAIL & RECORDS MGMT
1 (PDF)	GOVT PRINTG OFC A MALHOTRA
9 (PDF)	US ARMY RSRCH LAB PAMELA CLARK RDRL CIE S CHATT WILLIAMSON JOHN NOBLE SANDRA COLLIER MARK COLEMAN RDRL SES JOHN EICKE RDRL SES P MIKE SCANLON STEVE TENNEY WC KIRKPATRICK ALBERTS II